Revealing statistically robust strain rate effects on mechanical performance of pristine single fiber aramids

Atik Faisal[1], Alexander K Landauer[2], Walter Adamy Jr[1], Dumbari David Kabari[1], Kathleen A. Lamkin-Kennard[*1], Amanda L. Forster[2], Amy Engelbrecht-Wiggans[1]

1. Rochester Institute of Technology, Rochester, New York, USA
2. National Institute of Standards and Technology, Gaithersburg, Maryland, USA

*Corresponding author; kaleme@rit.edu

Atik Faisal ORCiD 0000-0003-2221-5320

Alexander K. Landauer ORCiD 0000-0003-2863-039X

Amanda L. Forster ORCiD 0000-0001-7397-4429

Keywords: Aramid fibers; Tensile testing; Strain rate sensitivity; Kolsky bar; High strength fiber; Body Armor; High strain rate

Abstract

High-performance synthetic fibers, especially aramid fibers, are widely used for body armor applications for their strength, stiffness, and excellent strength-to-weight ratio. Among those, Kevlar and Twaron (hereafter Aramid A and Aramid B, respectively) are extensively used for their superior thermal stability, high modulus, and proven ballistic performance. However, their tensile behavior under high strain rate (HSR) conditions approaching ballistic impact rates remains insufficiently characterized due to experimental challenges in measuring stress and strain at break at the single-fiber level. Previous studies have suggested moderate strain rate sensitivity in aramid-based fibers, but small sample sizes and limited accuracy in failure strain measurement under HSR have constrained the statistical robustness of the findings. In this study, a custom single-fiber tensile Kolsky bar instrument was configured for HSR tensile testing with accurate specimen alignment, gripping, and pulse quality. A rigid-body digital image correlation (DIC) method was implemented to track relative grip displacements and measure the strain at failure, enabling accurate measurements of failure force, strain, and strain rate at the single-fiber level. Using 62 samples per fiber at HSR and 100 per group under quasi-static (QS) conditions, clear strain-rate-dependent strengthening was observed in both fiber types. Maximum force, failure stress, and failure strain increased by approximately 28.5 % to 35.6 % under HSR compared to QS. The large sample size enabled a statistically robust assessment using distributional and non-parametric analyses, showing that Aramid B exhibited more uniform failure distributions than Aramid A. The approach establishes a practical framework for quantifying single-fiber strain-rate sensitivity.

1. Introduction

Ballistic-resistant, flexible body armor, often referred to as soft body armor, is critical for protecting emergency responders, including military personnel, police officers, firefighters, and emergency medical responders. According to the International Association of Chiefs of Police and the DuPont Kevlar Survivors' Club, body armor has saved over 3100 officers since 1975 [1]. Body armor effectiveness is commonly assessed using the destructive ballistic limit (V_{50}) test, defined as the projectile velocity at which penetration occurs in 50 % of cases [2]. Soft body armor typically consists of multi-layered fabrics or flexible fiber composites. Among the fibers used in body armor, poly-paraphenylene terephthalamide or PPTA, was first developed by DuPont in the 1960s and marketed as Kevlar[1] [3]. A similar aramid fiber with the same chemical structure, Twaron, was subsequently developed by Teijin [4]. These are the most common aramid fibers used in flexible body armor today, composed of highly oriented PPTA molecular chains with para-linkages that provide high axial strength and stiffness, making the fibers highly anisotropic [5], [6] and thermally stable, with decomposition around 500 °C [7], [8]. The ballistic performance during V_{50} testing of this class of armor largely derives from the mechanical performance of individual fibers during tensile loading [9]. However, fibers within the impact zone also experience complex multiaxial loading, including transverse compression, shear, and localized axial compression [10], [11]. Because PPTA fibers are much weaker in compression than in tension, compressive deformation can produce kink-band formation and fibrillation that reduce the residual tensile strength of the fibers [12], [13]. While this compressive behavior plays a direct role in energy dissipation and governs how much tensile capacity can be realized at the impact site [8], [11], axial tension remains the dominant mechanism and ultimate failure mode [8]. Consequently, ultimate tensile properties remain the primary inputs for ballistic performance models and are the focus of this work.

Mechanical performance characterization of body armor fibers is often conducted under quasi-static (QS) conditions, many orders of magnitude slower than the strain rates experienced during ballistic impacts. Since the polymer fibers exhibit viscoelasticity, a number of studies have examined the effect of strain rate using high strain rate (HSR) tensile testing methods to characterize the response of ballistic fibers under more realistic loading conditions. To study single fiber behavior under HSR conditions, the split Hopkinson (Kolsky) pressure bar technique was adapted by several groups for single fiber tensile testing [14]. Studies using similar systems on PPTA-based aramid fibers showed a modest effect on tensile strength, modulus, and toughness, increasing as strain rate increased [15], [16], [17], [18], [19], [20]. However, the magnitude, consistency, and statistical robustness of the reported rate effects in aramid fibers remain less clear. For example, Cheng et al. [19] reported only about 4 % increase in strength for Kevlar KM2. Others, such as Kim et al. [18] found an approximately 14 % increase, while Lim et al. [16] observed 6 % to 12 % increases across three aramid fiber types, and Sanborn and Weerasooriya [20] reported an 18.6 % increase for unwoven Kevlar KM2 fibers, based on mean failure stress values of (4.30 ± 0.49) GPa at QS rate and (5.10 ± 0.41) GPa at HSR.

[1] Certain equipment, instruments, software, or materials are identified in this paper in order to specify the experimental procedure adequately. Such identification is not intended to imply recommendation or endorsement of any product or service by the National Institute of Standards and Technology, nor is it intended to imply that the materials or equipment identified are necessarily the best available for the purpose.

Aramid fiber rate sensitivity and viscoelasticity arise through a combination of mechanisms during tensile loading from the anisotropy crystallinity introduced during the drawing process and the presence of both covalent bonds and weaker secondary bonds [21]. The covalent bonds within the molecular chains deform elastically, while secondary bonds undergo viscoelastic shear deformation. The secondary interactions weaken and eventually lead to fiber fracture as shear stress increases [22]. During tensile loading under HSR, molecular chains have insufficient time for rearrangement, leading to reduced intermolecular slip. As a result, fewer hydrogen bonds between adjacent PPTA chains break and more load transfers to primary covalent bonds, increasing the likelihood of covalent bond rupture and crystallite fracture [23], [24]. Scanning electron microscopy (SEM) observations by Tan et al. [24] support this, showing longer fibrils at low strain rates and shorter fibrils at about 1000 s^{-1}, consistent with a shift from secondary to primary bond failure. Since primary bond scission requires greater strain energy than secondary bond failure, this transition can also lead to higher failure strains at elevated loading rates [24]. The shift in load-bearing behavior results in a transition from viscoelastic to elastic behavior at HSR [8].

Prior studies have generally had limitations, including small sample sizes (typically between 10 and 16 specimens at HSR), indirect strain measurement techniques, and a lack of direct comparison to fiber-matched QS testing and diameter measurements [16], [18]. To overcome these limitations, in this work, extensive QS fiber testing was paired with testing on a specialized miniaturized Kolsky tension bar [25], known as the "Mini-Kolsky Bar," specifically designed for HSR tensile testing of single fibers. The main contribution of this work is a set of methodological advances that improve the accuracy and statistical robustness of single-fiber HSR characterization and comparison to lower rate testing. First, the NIST Mini-Kolsky Bar configuration was optimized, and a paper-frame templating technique was used to reduce grip-induced compliance, eliminate localized slipping, and minimize slack and gauge-length artifacts. Second, a rigid-body digital image correlation (DIC) method was implemented to measure grip displacement and failure strain directly, rather than deriving strain indirectly from bar signals as in most prior work. Third, failure stress was obtained using a paired-sampling approach with propagated measurement uncertainty, enabling for the first time a direct fiber-matched comparison between QS and HSR conditions. For high-strength single-fiber testing, at least 100 samples are preferable to ensure statistical robustness [26], and thus this study employed substantially larger sample sizes than prior work ($n = 62$ per fiber at HSR, $n = 100$ per QS condition) to provide a statistically robust characterization of rate-dependent mechanical behavior. Because these advances are not specific to PPTA, this approach is broadly applicable to HSR tensile characterization of other high-performance single fibers. By improving the accuracy and dataset size of single-fiber Kolsky bar testing methods for PPTA, the work aims to contribute to the development of lighter, more flexible, and more effective body armor systems.

2. Materials and Methods

The PPTA fibers, Aramid A and Aramid B, used in this study, were collected from Goodfellow Cambridge Limited (London, UK).

Table 1 provides a summary of the scientific nomenclature, tex numbers, and filament characteristics. Filament diameter is reported in

Table 1 as both the nominal manufacturer value and the mean diameter measured by SEM in our previous study [27]. The SEM measurements agree with diameters independently derived from FAVIMAT+ linear density. The manufacturer value is included for reference only. All mechanical property calculations use the measured linear density rather than the nominal diameter. The “tex” unit refers to the linear density of fibers or yarns and is a derived unit defined as the mass in grams per 1000 meters of length (1 tex = 10^{-6} kg/m; 1 dtex = 10^{-7} kg/m). Throughout this manuscript, linear density values are reported in the base SI unit (kg/m). Figure 1 shows SEM micrographs of the fibers, offering visual insight into the fiber structure. The fibers were stored as bundles on spools under ambient lab conditions (typically about 21 °C, 40 % relative humidity). To prevent degradation from ultraviolet (UV) light, the fiber spools were stored away from any UV light source [28].

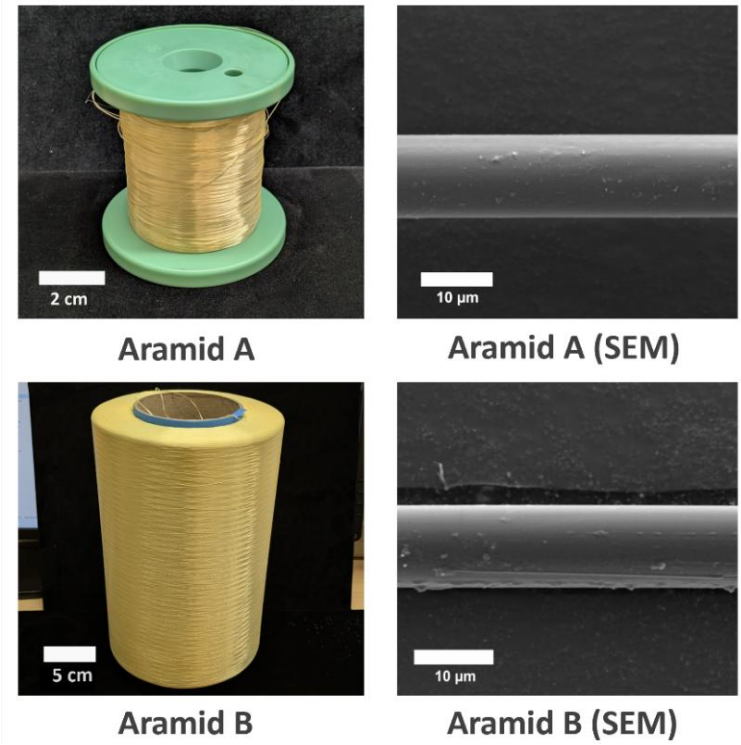

Figure 1: Optical images of the spools of Aramid A and Aramid B as received from the manufacturer (left column), with characteristic SEM micrographs of the filaments (right column).

Table 1: Overview of examined fibers.

Fiber Name (Commercial Name)	Scientific Nomenclature	Filament Diameter (nominal)	Filament Diameter (measured, SEM) [27]	No. of Filaments in Bundle	Linear density ($\times 10^{-6}$ kg/m)
Aramid A (Kevlar)	Polyparaphenylene	0.017 mm	(11.7 ± 0.1) µm	130	22 (tex)
Aramid B (Twaron)				550	55 (tex)

2.1 Single-Fiber Tension Kolsky Bar

The Mini-Kolsky Bar was specifically developed for HSR tensile testing of single fibers. The miniaturized system is inspired by foundational work conducted by various research groups, such as Chen

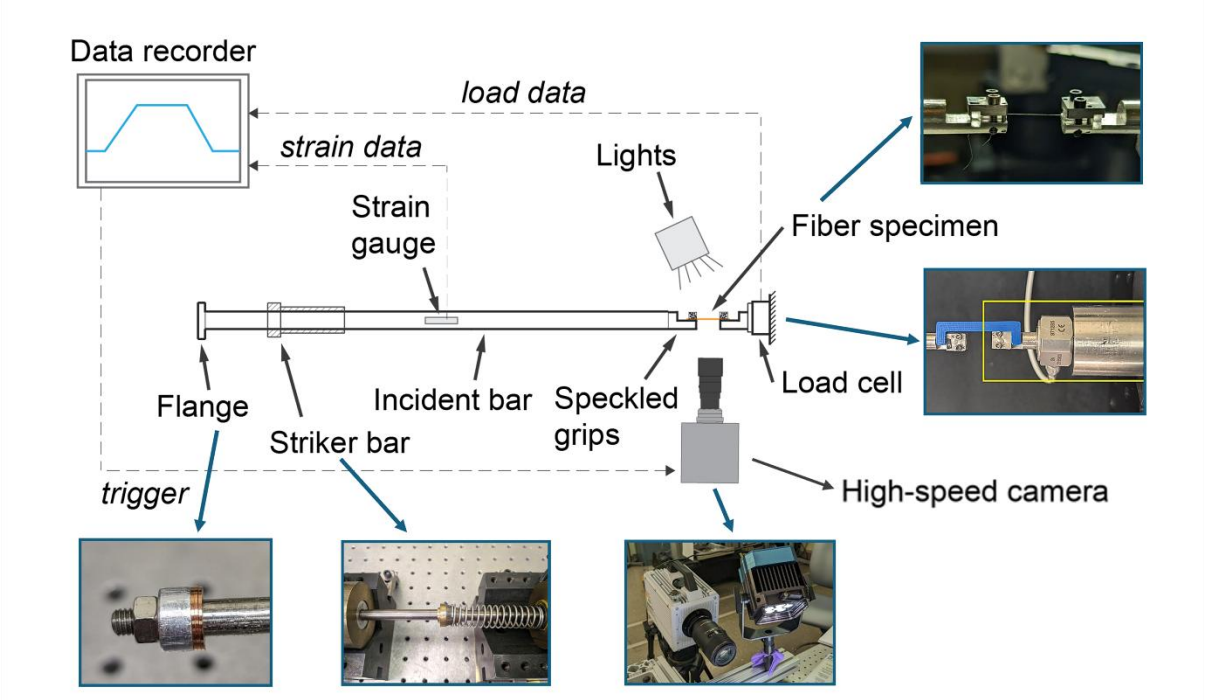

Figure 2: Schematic of the Mini-Kolsky Bar setup used for HSR tensile testing of single fibers.

et al. [25]. As shown in Figure 2, the system consists of the following key components: (1) a 75 cm long steel incident bar (6.35 mm diameter) with a flange at one end, which transmits the tensile stress wave to the fiber specimen; (2) a hollow brass striker tube driven by a compressed spring, which impacts the end flange (with pulse shaper attached) of the incident bar to generate a controlled tensile stress wave pulse; (3) a strain gauge mounted on the incident bar in conjunction with a Wheatstone bridge circuit, which records the incident strain signals as a function of time; (4) a quartz-piezoelectric load cell (Kistler 9712B5; Kistler Group, Winterthur, Switzerland; capacity 22.24 N, uncertainty ±1.0 %), which replaces the conventional transmission bar used in standard Kolsky bar configurations; and (5) a direct fiber gripping system consisting of two poly(methyl methacrylate) (PMMA) clamping blocks that clamp the fiber at a gauge length of approximately 10 mm without the use of adhesives. To conduct HSR tensile testing of single fibers, the National Institute of Standards and Technology (NIST) Mini-Kolsky Bar was modified to shape the pulse wave and obtain sufficient and repeatable impact velocity from the striker to enable fiber failure during the first loading pulse. To measure failure strain and strain rate, a high-speed camera was used to track the displacement of the speckled grips. The schematic of the Mini-Kolsky Bar setup is shown in Figure 2.

2.1.1 Constant Strain Rate

Achieving a constant strain rate in Kolsky bar experiments is technically challenging due to the open-loop nature of the system, in which the loading pulse is determined by the striker impact and pulse shaper rather than actively controlled through real-time feedback during the test. Constant strain rate deformation

ensures reliable material characterization by maintaining a uniform deformation rate over time. A uniform deformation rate is critical, producing consistent and comparable stress-strain data for strain-rate-sensitive materials [14]. To achieve this, a number of copper disks with an inner diameter of (6.50 ± 0.05) mm and an outer diameter of (10.90 ± 0.05) mm, and thicknesses of (0.80 ± 0.05) mm and (1.30 ± 0.05) mm were employed as pulse shapers, as shown in Figure 3(b). Uncertainties here represent measurement tolerances. The primary objective of pulse shaping is to extend the rise time of the stress pulse, promoting early stress equilibrium. Pulse wave shaping also ensures that stress develops in a way that produces uniform strain rate over time in a sample.

Figure 3(a) shows a representative force signal measured using a piezoelectric load cell (Kistler 9712B5) with a capacity of 22.24 N, installed in place of the transmission bar to directly measure the force. Since the transmitted tensile force in the single-fiber tests is less than 1 N at failure for the fibers tested, the 22.24 N full-scale load cell provided a sufficient load range while maintaining good sensitivity. In addition, Figure 3(c) shows a strain gauge voltage recorded during testing, which demonstrates the generation of a trapezoidal-shaped stress pulse, confirming the effectiveness of the pulse shaper. Note that this signal is used only for triggering the system and qualitative assessment of the pulse dynamics.

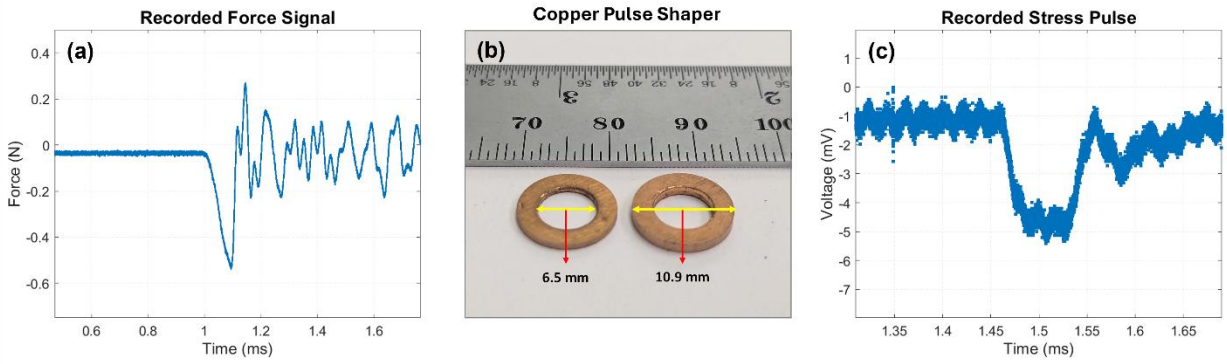

Figure 3: (a) Representative force-time signal measured using a piezoelectric load cell during Kolsky bar testing of a single fiber. (b) Copper pulse shapers used to shape the incident pulse, with an inner diameter of (6.5 ± 0.05) mm and an outer diameter of (10.9 ± 0.05) mm. (c) Recorded strain gauge voltage signal showing a trapezoidal-shaped stress pulse.

2.1.2 Pulse Duration Optimization

To ensure the fiber breaks within the first pulse in the Kolsky bar setup, sufficient velocity and pulse duration from the striker bar were required. The striker bar length, L, directly influences the pulse duration T according to

$$T = \frac{2L}{C_{st}} \tag{1}$$

where C_{st} is the elastic wave speed of the striker material [14]. A longer striker bar increases T, ensuring the pulse duration is adequate for fiber failure. Based on trials using different striker bar lengths and monitoring force-time responses, a striker bar length greater than 220 mm ensured breakage occurred within the first stress wave. This length was used for all subsequent tests. Additional details related to optimization of the striker bar length are provided in the Supplementary Material (Figure S1).

2.2 Strain Measurement Using a Custom DIC Setup

Accurate strain measurement is essential for characterizing the dynamic behavior of fibers under HSR conditions. In this study, a custom rigid body motion measurement of the grips using DIC was utilized for strain measurements. A Photron FASTCAM SA5 operated at 124 000 frames per second (fps) with a reduced field of view (576 pixels × 88 pixels) was used to keep the grips in view with sufficient spatial and temporal resolution for the rigid body DIC to capture the grip displacements.

Strain at failure was calculated directly by measurement of the relative motion between the moving left grip and the stationary right grip obtained from high-speed images. Speckle patterns were painted onto both the left and right grips on both sides. Painted grips with DIC region of interest are shown in Figure 4. The rigid body motion of each grip was tracked using the q-factor-based digital image correlation (qDIC) algorithm in incremental mode, and the median horizontal displacement within each grip ROI was taken as the grip motion for that frame. This algorithm was adapted from Landauer et al. [29]. Key qDIC settings relevant to the rigid body motion tracking are provided in Table 2. The custom DIC procedure was calibrated by applying known displacements to the left grip using a manual positioning device. The qDIC-measured displacement was then compared against a nominal displacement. Speckle patterns were painted on both grip sides and evaluated independently. Additional calibration details and comparison plots are provided in Supplementary Figure S2 and Figure S3.

Figure 4: Speckle-patterned left and right grips used for rigid-body DIC tracking. The highlighted boxes indicate the DIC regions of interest (ROIs) used to measure the relative grip displacement.

The relative displacement, ΔL, was obtained as the cumulative difference between the displacements of the moving left grip and the stationary right grip. The approach avoids uncertainties associated with indirect strain measurements from bar signals or laser systems, providing more reliable data at the single-fiber level. Because the analysis was performed incrementally from frame to frame, the total grip displacement was obtained by summing the successive displacement increments over the full image sequence. Engineering strain, ε, was then calculated as

$$\varepsilon = \frac{\Delta L}{L_0} \tag{2}$$

where L_0 is the specimen-specific initial gauge length. The initial gauge length of each sample was measured from the distance between the inner edges of the left and right grips from the static image before displacement since the mounting of a fiber template might change the gauge length. The strain rate, $\dot{\varepsilon}$, for each test was obtained by numerical differentiation of the strain-time history, $\dot{\varepsilon} = d\varepsilon/dt$, using the "gradient" function in MATLAB (Mathworks, Inc., Natick, MA).

To synchronize the optical and force measurements, the onset of deformation was identified as the first camera frame at which the calculated strain rate exceeded ten times the standard deviation of the initial baseline frames. This criterion was used to identify true fiber loading and to exclude baseline noise and initial slack. The 10× threshold was selected after testing several thresholding approaches and was found to provide a stable onset identification above the toe region and at the start of primary loading. While the selection was empirical, it was found to be robust across the dataset, producing consistent onset identification without introducing identifiable timing-related artifacts. The camera time base was then shifted to account for wave propagation time from the strain gauge location to the grips in the incident bar. The force history was interpolated onto the camera-frame time base, and the failure strain was defined as the engineering strain at the frame corresponding to the maximum tensile force. This assumes the fiber breakage occurred at the force peak during the first loading pulse. The method assumes that all grip motion contributes directly to fiber strain, disregarding grip slippage [30], [31]. A similar image-based displacement-tracking approach has also been reported by Koumlis and Lamberson [32].

Table 2: Key qDIC settings relevant to this rigid body motion tracking.

Parameters	**Value**
Region of interest (ROI) (approx.)	55 pixels × 175 pixels
Type	Local DIC
Pixel-to-Millimeter conversion	0.0434 mm/px
Camera noise	0.03 % full scale
Displacement resolution (mean ± SD)	(0.0086 ± 0.0004) mm

2.3 Quasi-static and HSR Tensile Testing

Systematic QS testing was conducted on single fibers using a FAVIMAT+ Automated Single Fiber Tester (Textechno, Germany). Testing conditions of 0.1 mm/min, 1 mm/min, 1.5 mm/min, and 6 mm/min were selected to capture a comprehensive overview of the influence of strain rate on single fibers failure force and strain (and the resulting failure stress) in the low-rate regime. Testing conditions of 1 mm/min and 1.5 mm/min within the QS regime were included to assess whether small differences in strain rate produce measurable changes and to align with one condition (1.5 mm/min) in the ASTM C1557 standard. The equivalent strain rates are provided in Table 3. A gauge length of 15 mm was used for QS testing using the FAVIMAT+. HSR testing was conducted using the NIST Mini-Kolsky Bar. A gauge length of 10 mm was used for HSR testing. A 10 mm gauge length was chosen as the longest length that reliably produced fiber failure within the first strain pulse while maintaining a repeatable pulse for the current setup. Shorter gauge lengths helped ensure sufficient displacement to reach fiber failure and increased the effective strain rate, bringing it closer to ballistic rates. Since the utilized setup relied on a manual spring mechanism to strike the bar, the applied strain rate was not constant for each test. Therefore, the strain rate was calculated for each experiment from the measured strain-time history. Across the HSR datasets ($n = 62$ per fiber), the mean measured strain rate was approximately 370 s^{-1}, with most tests falling between 350 s^{-1} and 400 s^{-1}. These tests therefore represent a single high-rate condition rather than a continuous range of HSR. As this rate is orders of magnitude above the QS conditions it is sufficient to reveal differences between QS and HSR loading, but remains below the extreme rates of ballistic impact, where additional mechanisms such as adiabatic heating, shock effects, and altered macromolecular deformation may influence fiber response [33]. The rate-dependent trends reported here should therefore

be interpreted within this moderate high-rate regime and care should be taken with any extrapolation to extreme ballistic conditions. For HSR tests, specimens were mounted without slack. However, no controlled or measurable pretension was applied due to the open-loop configuration. A summary table of QS testing and HSR testing parameters is provided in Table 3.

Table 3: Summary of QS and HSR tests for Aramid A and Aramid B, including the testing parameters and number of samples tested per material for each condition.

Testing Device (Testing Condition)	Gauge Length (nominal) (mm)	Nominal Tensile Testing Parameters			No. of samples tested (per material)
		Testing conditions/ Loading rate (mm/min)	Equivalent strain rate (s^{-1})	Pretension (cN/tex)	
FAVIMAT+ (QS)	15	0.1	1.11×10^{-4}	0.5	100
FAVIMAT+ (QS)		1.0	1.11×10^{-3}	0.5	100
FAVIMAT+ (QS)		1.5	1.67×10^{-3}	0.5	100
FAVIMAT+ (QS)		6.0	6.67×10^{-3}	0.5	100
Kolsky (HSR)	10	2.22×10^{5}	3.7×10^{2}	N/A	62

2.4 Sample Preparation

Single fibers were prepared slightly differently for tensile testing under QS and HSR strain rates. For QS testing using the Automated Single Fiber Tester (FAVIMAT+), fiber bundles approximately 25 mm in length (effective gauge length of 15 mm) were cut from continuous bundles as depicted in Figure 5. For

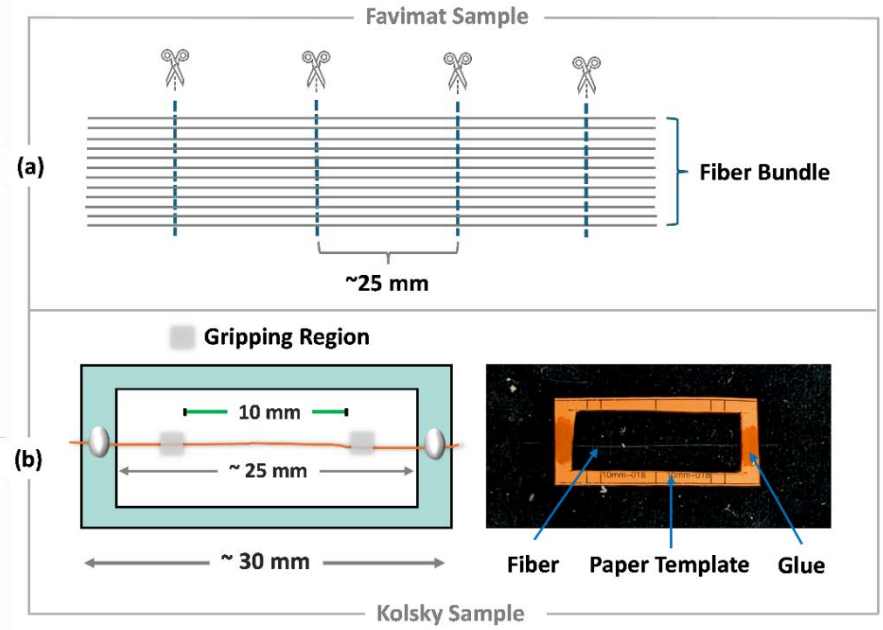

Figure 5: Schematic of sample preparation for single-fiber tensile testing. (a) Sample for QS testing using the FAVIMAT +: fiber bundles (approximately 25 mm) were cut, and individual fibers were isolated to provide an effective gauge length of 15 mm. (b) Sample for HSR testing using the Kolsky bar: a paper template with a rectangular cutout was used to mount the fibers to provide an effective gauge length of 10 mm. The indicated gripping region is not drawn to scale.

HSR testing using the Kolsky bar setup, a different mounting approach was necessary based on the gripping system and setup. Paper templates of approximately 30 mm length were prepared, featuring a rectangular cutout design as seen in Figure 5. Single fibers of approximately 30 mm length were separated from bundles and then mounted onto the templates without stretching, to ensure as little slack or preload as possible. Cyanoacrylate glue was applied to securely fix the fiber onto the template. The templates were stored for about one hour to allow for full curing of the adhesive prior to testing. The detailed schematic of this preparation method is illustrated in Figure 5.

For the calculation of failure stress under HSR conditions, linear density was measured using the FAVIMAT+ on an adjacent section of the same filament from which the HSR specimen was prepared. Specifically, single filaments were separated from the 30 mm bundle and mounted in the paper frame template for HSR testing, while a neighboring portion of the same filament was set aside for linear density measurement on the FAVIMAT+. This approach was supported by findings from our earlier study [27], which showed that linear density varies less along an individual fiber than among randomly selected fibers within a bundle. The measured linear density was then used to calculate the fiber cross-sectional area for failure stress calculation according to $A = Tt/\rho$ where T_t is the measured linear density and ρ is the nominal volumetric density (1.44 g/cm^3) of PPTA. This approach assumes a uniform material density along and across the fiber, while the paired-sampling approach assumes that the adjacent segment has a representative cross-sectional area of the tested gauge section. These assumptions were validated in our earlier study of this type of PPTA fibers [27], in which the fiber diameter derived from FAVIMAT+ linear density agreed with direct SEM measurements within experimental uncertainty. The method allows estimation of fiber stress under HSR loading without requiring direct diameter measurements for each Kolsky-tested sample.

3. Results and Discussions

3.1 Sample Uniformity

To evaluate whether linear density influenced mechanical responses, its relationship with maximum force, failure strain, and failure stress was first examined at a testing condition of 1.5 mm/min (Supplementary Figure S5). For Aramid A, a strong positive correlation was observed between linear density and maximum force ($R^2 = 0.65$), while moderate to weak correlations were observed with failure strain ($R^2 = 0.14$) and failure stress ($R^2 = 0.03$). In contrast, Aramid B exhibited weaker correlations across all three metrics ($R^2 = 0.13$, 0.00, and 0.03, respectively). As expected, maximum force increased with linear density, whereas failure stress, calculated by normalizing force by the fiber cross-sectional area showed minimal dependence on linear density. The results indicated that linear density had little to no influence on strain and stress behavior.

Although strain and stress were largely independent of linear density, as expected, it was still important to ensure that fiber selection was statistically consistent across groups to avoid any potential bias in rate-dependent comparisons. Therefore, a one-way ANOVA was conducted for each fiber type on linear density values from the five different testing condition groups (0.1, 1, 1.5, and 6 mm/min, and HSR). The one-way ANOVA was chosen after confirming that linear density data were normally distributed and satisfied the homogeneity of variance assumption (Brown-Forsythe test: $p = 0.95$ for Aramid A and $p = 0.07$ for Aramid B). The complete ANOVA results are summarized in Supplementary Table S1. For Aramid A, no significant differences are observed among the five groups ($F = 1.27$, $p = 0.28$). Similarly,

Aramid B shows no significant variation ($F = 2.11$, $p = 0.08$). These results confirm that linear density is statistically consistent across loading-rate groups, suggesting that selection bias is unlikely to influence any observed rate-dependent trends.

To visualize the distribution of linear density across all five test conditions, including the HSR condition, violin plots are shown in Figure 6. For both Aramid A and Aramid B, the violin plots show similar median values and interquartile ranges (IQRs) across all groups. The linear density values for Aramid A span $[1.2, 2.2] \times 10^{-7}$ kg/m, with median values remaining close to 1.6×10^{-7} kg/m. The linear density values for Aramid B span $[0.9, 1.3] \times 10^{-7}$ kg/m, with much tighter distributions than are observed for Aramid A. To quantify these visual trends, summary statistics for each testing condition are reported in Table 4. For Aramid A, the mean linear density falls between 1.60×10^{-7} kg/m and 1.64×10^{-7} kg/m, and for Aramid B between 1.04×10^{-7} kg/m and 1.06×10^{-7} kg/m. In both cases, the variation between mean values across testing conditions is smaller than the within-group standard deviation, indicating that the means are statistically consistent across testing conditions for both fibers. The SDs for Aramid A groups range from 0.18×10^{-7} kg/m to 0.19×10^{-7} kg/m, whereas for Aramid B they range from 0.05×10^{-7} kg/m to 0.07×10^{-7} kg/m. The corresponding coefficients of variation (CV) values are about 11 % to 12 % for Aramid A and about 5 % to 7 % for Aramid B. These results show that while both fibers exhibit statistically consistent mean linear density across testing conditions, Aramid B has a tighter underlying distribution (lower SD and CV) than Aramid A. Overall, the violin plots and the consistent statistics indicate the fiber selection was uniform across different test conditions.

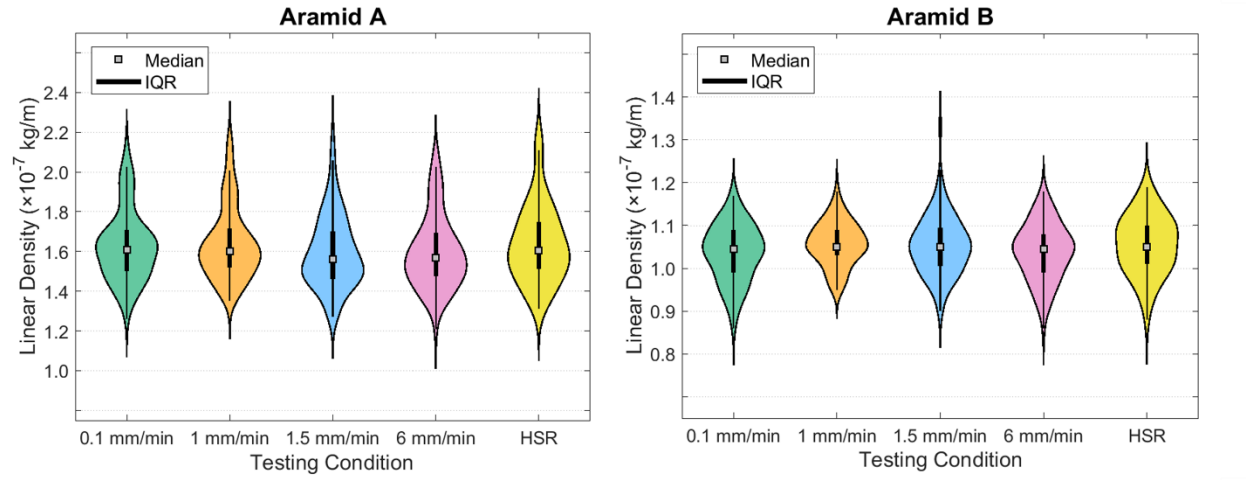

Figure 6: Linear density distributions for Aramid A and Aramid B across five test conditions: four QS extension rates ([0.1, 1, 1.5, 6] mm/min, and HSR (2.22×10^5 mm/min), corresponding to nominal strain rates of [1.1×10^{-4}, 1.1×10^{-3}, 1.7×10^{-3}, 6.7×10^{-3}] s^{-1}, respectively) and the HSR condition (370 s^{-1}).

Although Aramid A and Aramid B have the same chemical composition (PPTA), the narrower linear density distribution of Aramid B likely reflects differences in manufacturing and processing history. The fibers were produced by different manufacturers and had different spool formats, with Aramid B originating from a larger spool with a higher filament count. While the average filament diameters are similar, the broader variability of Aramid A may be associated with differences in filament uniformity, localized geometric variations, or defect populations arising from manufacturing and handling history.

This interpretation is consistent with the higher variability observed in the failure properties of Aramid A compared with Aramid B.

Table 4: Summary statistics (n = 100 for QS; n = 62 for HSR) of linear density for Aramid A and Aramid B across testing conditions. Reported values are the mean and standard deviation (SD) in $\times 10^{-7}$ kg/m, and CV for each group.

Fiber	Statistics	Nominal Testing Conditions				
		0.1 mm/min	1 mm/min	1.5 mm/min	6 mm/min	HSR (2.22×10^5 mm/min)
Aramid A	Mean ($\times 10^{-7}$ kg/m)	1.63	1.64	1.60	1.60	1.64
	SD ($\times 10^{-7}$ kg/m)	0.18	0.18	0.18	0.19	0.19
	CV (%)	11.11	11.16	11.55	11.67	11.82
Aramid B	Mean ($\times 10^{-7}$ kg/m)	1.04	1.06	1.05	1.04	1.06
	SD ($\times 10^{-7}$ kg/m)	0.07	0.05	0.07	0.07	0.07
	CV (%)	6.43	4.85	6.53	6.42	6.44

3.2 Failure Strain

3.2.1 Weibull Analysis

The Weibull distribution is commonly used to characterize the failure distribution of fibers and fiber-reinforced composites [34]. The rate-dependent maximum force results, analyzed using the same Weibull and statistical framework, are provided in Supplementary Section 2.2. In Figure 7(a-b), the rate-dependent distribution of strain at failure is illustrated using two-parameter Weibull probability plots for Aramid A and Aramid B. Weibull scale (η) and shape (β) parameters were estimated using maximum likelihood estimation (MLE) via the MATLAB fitdist function, with 95 % confidence intervals (CIs) obtained from the parameter covariance matrix. Figure 7(c-d) show the corresponding scale (η) and shape (β) parameters against different testing conditions. The scale parameter represents the characteristic scale of the Weibull distribution. In contrast, the shape parameter determines the shape of the distribution and indicates the degree of variability relative to the scale parameter. Higher values of the shape parameter indicate a narrower failure distribution [35].

The failure strain distributions for Aramid A and B show a clear rightward shift when comparing HSR to the QS testing conditions, as seen in Figure 7(a-b) indicating an increase in failure strain with strain rate. Within the QS regime, the distributions largely overlap, suggesting minimal strain rate sensitivity among the QS testing conditions. The trends observed in the Weibull parameter plots provide further insight into rate-dependent effects on fiber failure strain. Figure 7(c) shows that for Aramid A, the scale parameter (η) increases from 3.77 % [95 % CI: 3.71 % to 3.82 %] at 0.1 mm/min to 5.10 % [4.97 % to 5.23 %] under HSR, corresponding to a relative increase of 28.5 % to 35.3 % from the QS testing. Similarly, for Aramid B, the scale parameter increases from 3.82 % [3.77 % to 3.87 %] at 0.1 mm/min to 5.18 % [5.05 % to 5.32 %] under the HSR testing condition (a 35.6 % increase). Reported intervals represent the 95 % CIs of the MLE fit (see Supplementary Table S4). The increase in characteristic failure strain with strain rate is consistent with the trends observed in the probability plots.

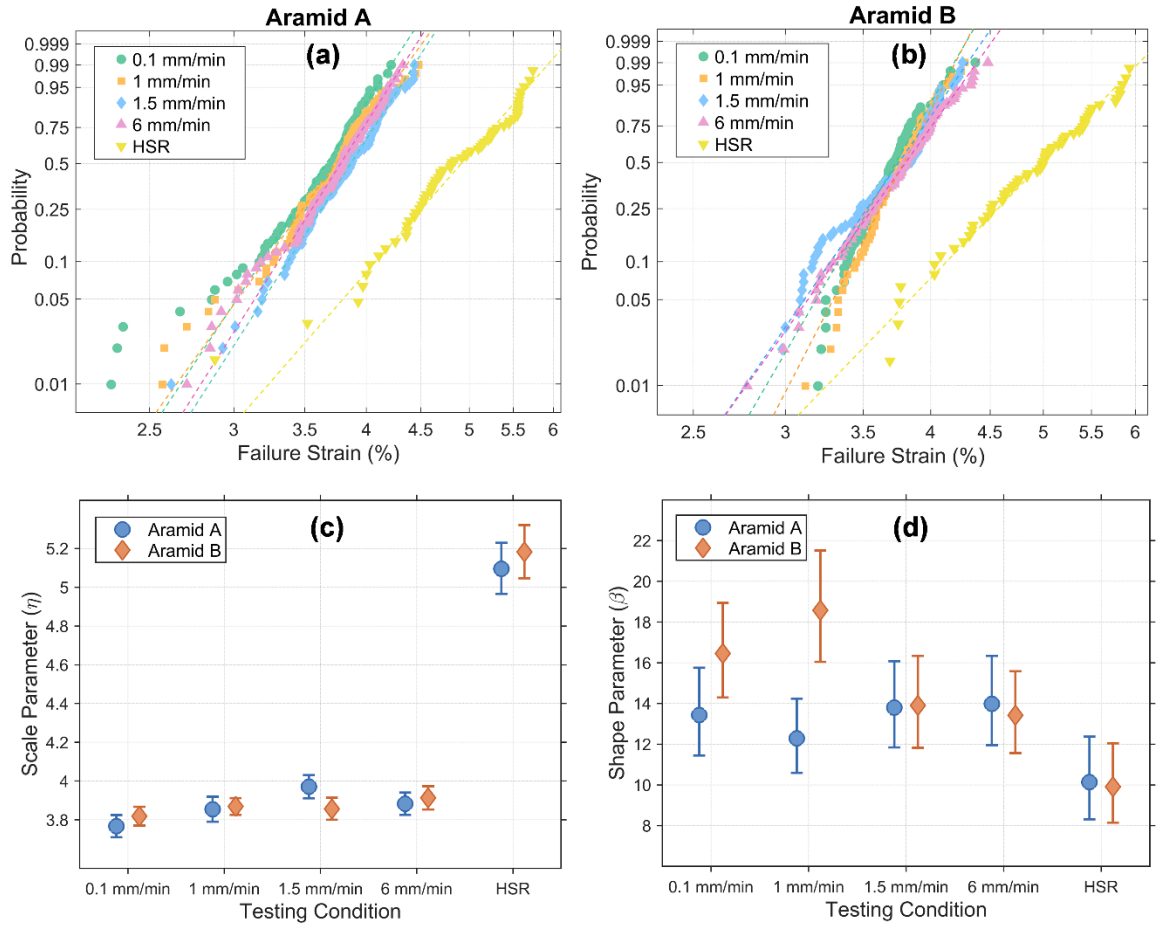

Figure 7: (a-b) Two-parameter Weibull probability plots of failure strain for Aramid A and Aramid B fibers tested under five different testing conditions ([0.1, 1, 1.5, 6] mm/min, and HSR), corresponding to nominal strain rates of 1.1×10^{-4} s^{-1}, 1.1×10^{-3} s^{-1}, 1.7×10^{-3} s^{-1}, and 6.7×10^{-3} s^{-1}, respectively) and the HSR condition (370 s^{-1}). Dashed lines represent Weibull fits to the data. (c-d) Weibull scale (η) and shape (β) parameters with 95 % CI for both fibers as a function of testing condition.

In Figure 7(a-b), the overall fit for all groups is consistent with the two-parameter model. The visual linearity of the points on the Weibull probability plots was used as a qualitative diagnostic for two-parameter fit adequacy. Quantitative goodness-of-fit tests were not applied, and the reported parameters and uncertainties are derived from MLE. However, the failure strain distribution for Aramid B at 1.5 mm/min appears slightly less linear below the median value. The minor deviation is likely due to sample variability or a weaker fit with the two-parameter model. For all testing conditions, including HSR, the lower-tail behavior is generally comparable. However, Aramid A shows a slightly more extended lower tail at 0.1 mm/min and 1 mm/min. This suggests that the slowest QS conditions for Aramid A include a slightly weaker subset of specimens contributing to the extended lower-tail behavior. The central portion of the distributions, however, remains similar across the QS testing conditions.

The lower-tail behaviors and overall fits are reflected in the Weibull shape parameter (β) trends shown in Figure 7(d). For Aramid A, β is slightly lower at 0.1 mm/min and 1 mm/min versus the other QS testing conditions, likely due to the extended lower-tail behavior. Under HSR loading, β decreases for both fibers. For Aramid A, β remains between 12.3 [10.6 to 14.2] and 14.0 [12.0 to 16.3] across the QS testing conditions but decreases to 10.1 [8.3 to 12.4] under HSR. Aramid B exhibits higher β values (ranging from 13.4 [11.6 to 15.6] to 18.6 [16.1 to 21.5]) in the QS regime and shows a similar decrease to 9.9 [8.1 to 12.1] under HSR loading. The narrower failure strain distribution compared with Aramid A is consistent with the lower linear density variability observed for Aramid B. Notably, Aramid B exhibits a distinct spike in β at the 1 mm/min condition (β = 18.6), which is also reflected in its low SD (0.2) and CV (6.0 %) in Table 5. Because this localized reduction in variability does not follow a systematic trend across the broader QS testing conditions, and the scale parameter shows no corresponding shift (Figure 7c), it is unlikely to represent a strain-rate effect. Instead, it most likely reflects sampling variability, with the tested fiber subset exhibiting fewer severe structural defects or localized geometric variations than the groups tested at the adjacent loading rates. The trends are also evident in Table 5, where the SD and CV increase slightly under HSR conditions. For instance, the SD for all QS conditions is 0.3 to 0.4 and rises to 0.6 under HSR loading for Aramid A, while for Aramid B it increases from 0.2 to 0.4 to 0.6. Similarly, the CV increases from ≈6 % to ≈10 % to ≈12 % for both fiber types. The broader failure strain distribution at HSR may be partly attributed to the inherent test-to-test variability in strain rate produced by the spring-driven striker mechanism of the Kolsky bar. Unlike the FAVIMAT+, which precisely controls crosshead speed, the Kolsky bar produces strain rates that vary across tests (approximately 350 s^{-1} to 400 s^{-1} in the present study). Since failure strain is rate-dependent [23], even modest strain rate variation across HSR tests introduces additional variability in the measured failure strain. This could contribute to the observed decrease in β and increase in CV at HSR.

Results from the Weibull plots are consistent with the summary statistics in Table 5. For both Aramid A and B, the mean failure strain under QS conditions ranges from 3.6 % to 3.8 %, increasing to 4.9 % under HSR loading. Overall, the Weibull analysis and summary statistics demonstrate a clear rate-dependent effect in failure strain, with higher failure strains observed under HSR conditions, while the QS testing conditions produce comparable results. The complete Weibull scale and shape parameters, with 95 % confidence intervals (CI) for both fibers, are provided in Supplementary Table S4.

Table 5: Summary of mechanical properties for Aramid A and Aramid B fibers tested at five different testing conditions. Mean, SD, and CV are reported for failure strain (%), and calculated failure stress (GPa).

	Properties	Statistics	0.1 mm/min	1 mm/min	1.5 mm/min	6 mm/min	HSR
Aramid A	Failure Strain (%)	Mean	3.62	3.70	3.82	3.74	4.85
		SD	0.38	0.36	0.34	0.34	0.59
		CV	10.45	9.76	8.93	9.19	12.16
	Failure Stress (GPa)	Mean	3.49	3.64	3.83	3.81	4.57
		SD	0.39	0.37	0.36	0.36	0.71
		CV	11.26	10.29	9.45	9.35	15.50
Aramid B	Failure Strain (%)	Mean	3.71	3.76	3.71	3.77	4.93
		SD	0.23	0.23	0.37	0.33	0.59
		CV	6.28	6.01	10.08	8.67	11.91
	Failure Stress (GPa)	Mean	3.63	3.74	3.68	3.86	4.81
		SD	0.27	0.23	0.39	0.34	0.52
		CV	7.47	6.09	10.48	8.75	10.87

3.2.2 Statistical Analysis

To assess statistical differences in failure strain among the different testing condition groups, a non-parametric Kruskal-Wallis test was performed, followed by Dunn's post hoc comparisons. The non-parametric approach was selected because the failure strain and failure stress data did not follow a normal distribution. The approach serves as a rank-based alternative to one-way ANOVA for comparing multiple groups [36]. A color-coded summary of statistically significant ($p < 0.01$) pairwise differences across all properties is provided in Table 6, and the full pairwise p-value matrix is provided in Supplementary Table S5.

Figure 8 shows failure strain as a function of testing conditions for Aramid A and Aramid B across the five testing conditions. Within the QS regime (0.1 mm/min to 6 mm/min), the median failure strain and IQR show no clear trend with testing conditions for either fiber type. The only exception is at the testing condition of 1.5 mm/min for Aramid A, which shows a slight upward shift in median failure strain relative to the other QS conditions. Kruskal-Wallis and post hoc analysis results, summarized in Table 6 and, Table S5 are consistent with the observed trends in Figure 8. For Aramid B, no statistically significant differences in failure strain are detected between any of the four QS testing conditions. For Aramid A, only one significant difference is observed between the testing conditions of 0.1 mm/min and 1.5 mm/min. Notably, the 0.1 mm/min vs 6 mm/min pair is not significant. This inconsistency and the lack of a clear monotonic trend across QS testing conditions suggest that the one significance observed is more likely due to normal scatter rather than a strain rate effect within the QS regime.

Higher median failure strains are observed under the HSR loading condition for both fiber types in comparison to all QS loading conditions. The higher observed failure strains are consistent with the distributions observed in the Weibull analysis. Table 6 also confirms that the failure strain at the HSR is statistically different (higher) than all four QS testing groups.

Before attributing the observed increase in failure strain to a strain-rate effect, it is important to consider potential differences between the QS and HSR testing setups, including gauge length, gripping, pretension, and displacement measurement. The QS and HSR tests used gauge lengths of 15 mm and 10 mm, respectively. Supplementary QS tests on 50 fibers of each type showed no significant difference in failure stress between the two gauge lengths (Figure S8, Table S6). The mean failure strain differed by only ~3 %, an order of magnitude smaller than the observed strain-rate effect. Both setups use direct mechanical clamping without adhesive, and prior work on the same Kolsky bar demonstrated linear stress-strain behavior to failure with negligible system compliance under HSR loading [22]. Although controlled pretension was not possible in the open-loop HSR configuration, specimens were mounted without slack, and the strain-onset criterion (Section 2.2) excludes any residual slack or toe region. Finally, engineering strain was determined in both systems from the relative grip displacement over the gauge length, differing only in the displacement measurement method. Collectively, these differences are unlikely to account for the observed increase in failure strain.

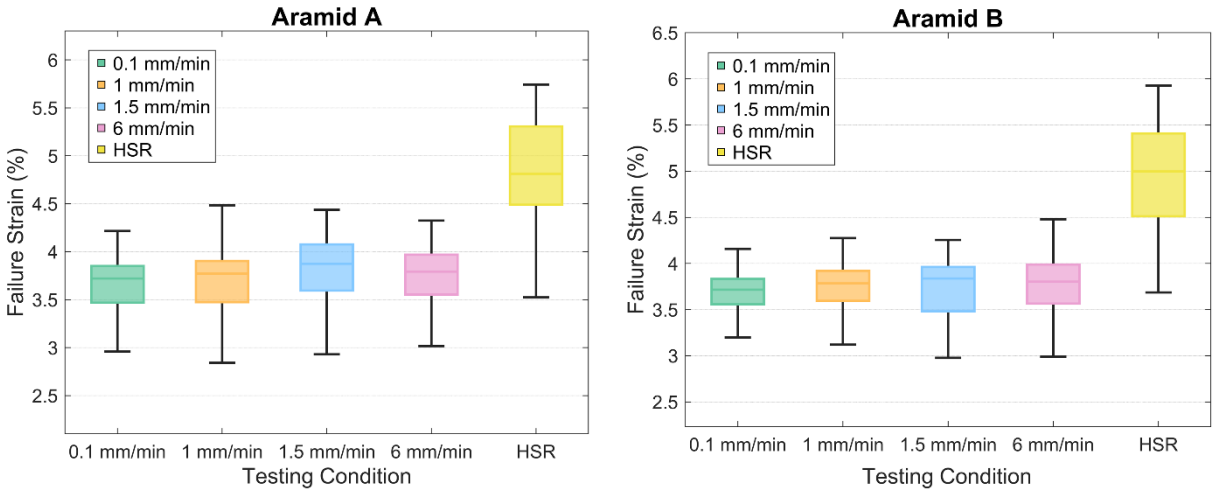

Figure 8: Box plots of failure strain for Aramid A and Aramid B across five different testing conditions ([0.1, 1, 1.5, 6] mm/min, and HSR), corresponding to nominal strain rates of 1.1 × 10^{-4} s^{-1}, 1.1 × 10^{-3} s^{-1}, 1.7 × 10^{-3} s^{-1}, and 6.7 × 10^{-3} s^{-1}, respectively) and the HSR condition (370 s^{-1}). The central line represents the median, the lower and upper box edges represent the 25th and 75th percentiles (IQR). The whiskers extend to the most extreme data points within 1.5 × IQR from the box edges. Outliers beyond the whiskers are not displayed.

With these setup-related factors ruled out, the observed increase is attributed to a genuine strain-rate effect. The present study characterizes the rate-dependent changes in failure strain and stress statistically and does not include direct fractographic or microstructural observation of the failure process. The mechanistic interpretation below is therefore drawn from the established literature and is offered to contextualize the measured trends rather than as direct empirical evidence from this work. Nevertheless, the observation is consistent with the rigid-rod microstructure of PPTA and supported by both computational and experimental studies. For example, Mercer et al. [23] used molecular dynamics simulations to show that the failure strain of PPTA crystallites increases with strain rate. They attributed this to stress-assisted thermal fluctuations, where at lower strain rates, thermal energy has more time to promote bond rupture at lower strain levels. Additionally, Tan et al. [24] observed using SEM imaging that fractured aramid specimens show long axial fibrils at low strain rates, which indicates inter-chain slippage and secondary bond failure. At HSR, the fibrils become shorter, suggesting a shift toward

primary covalent bond scission. The experimental results confirmed this, reporting a 26 % increase in failure strain at 480 s^{-1} relative to QS conditions for Twaron yarns (aramid), consistent with the present findings. It is noteworthy that these rate-dependent mechanisms may not be evident from fracture-surface morphology, as Kim et al. [18] reported largely indistinguishable fracture surfaces for PPTA fibers tested under QS and HSR loading. Rate-dependent differences become apparent only at the fibril scale [24]. Direct microstructural characterization across strain rates would therefore provide valuable complementary evidence and is left for future work. Notably, most prior single-fiber Kolsky bar studies on aramid fibers did not directly measure failure strain at HSR, instead deriving strain indirectly from bar signals or did not report it [16],[18], [19], [20].

Table 6: Color-coded summary of statistically significant ($p < 0.01$) pairwise differences from Kruskal-Wallis tests with Dunn's post hoc comparisons for the mechanical properties of Aramid A and Aramid B across testing conditions. Green cells with tick marks indicate statistically significant differences; blank cells indicate no significant difference.

Property	Fiber	HSR vs all QS	(0.1 vs. 1) mm/min	(0.1 vs. 1.5) mm/min	(0.1 vs. 6) mm/min	(1 vs 1.5) mm/min	(1 vs 6) mm/min	(1.5 vs 6) mm/min
Failure Strain	Aramid A	✓		✓				
	Aramid B	✓						
Failure Stress	Aramid A	✓		✓	✓	✓		
	Aramid B	✓			✓			

3.3 Failure Stress

3.3.1 Weibull Analysis

The Weibull probability plots depicting failure stress in Figure 9(a-b) show that both Aramid A and B fibers exhibit rate-dependent failure stress, which aligns with the earlier observations for failure strain and the maximum force results reported in Supplementary Section 2.2. For both fiber types, the HSR testing condition shows a distinct rightward shift, while the QS testing conditions display a smaller but consistent shift as the strain rate increases from 0.1 mm/min to 6 mm/min. The trend is consistent with the scale parameters (η) in Figure 9(c) and supplementary Table S4. For Aramid A, η increases from 3.65 GPa [3.59 GPa to 3.71 GPa] at 0.1 mm/min to 3.96 GPa [3.90 GPa to 4.02 GPa] at 6 mm/min, then increases sharply to 4.86 GPa [4.70 GPa to 5.03 GPa] under HSR testing conditions. Aramid B follows a similar trend, rising from 3.76 GPa [3.70 GPa to 3.81 GPa] to 4.01 GPa [3.94 GPa to 4.08 GPa], and reaching 5.03 GPa [4.91 GPa to 5.16 GPa] at the HSR testing condition. Reported intervals represent the 95 % CIs of the MLE fit (see Supplementary Table S4). The summary statistics in Table 5 are also consistent with the trends shown in scale parameter values. For Aramid A, the mean failure stress increases by 9.1 % across the QS range. A 30.8 % increase is observed between the failure stress obtained at the HSR testing condition vs. the rate of 0.1 mm/min. Aramid B shows a 6.3 % QS increase and a 32.4 % increase under the HSR testing condition. Together, the increases in failure stress with strain rates and the monotonic rise in η confirm that failure stress is strain-rate sensitive for both fiber types and is most pronounced under HSR.

Because HSR failure stress was calculated using diameter (derived from linear density) measured on an adjacent segment of the same filament rather than the tested segment itself, the associated measurement uncertainty was estimated using standard error propagation. The combined relative uncertainty accounts for both the load cell uncertainty (±1.0 %) and the intra-filament linear density variability. The linear density variability was estimated by averaging multiple measurements along individual filaments across a set of filaments. The CVs were approximately 6 % and 4 % for Aramid A and Aramid B, respectively. The detailed measurement methodology is described in [27]. The resulting propagated uncertainties are approximately 6.1 % and 4.2 % for Aramid A and Aramid B, respectively, which are substantially smaller than the observed 31 % to 32 % increase in failure stress from QS to HSR conditions. These relatively low uncertainties confirm that the rate-dependent differences are well outside the measurement uncertainty. Additionally, the lack of a controlled pretension under HSR conditions does not affect the reported failure stress, which is calculated from the peak force and pair-fiber measured cross-sectional area and is therefore independent of initial preload.

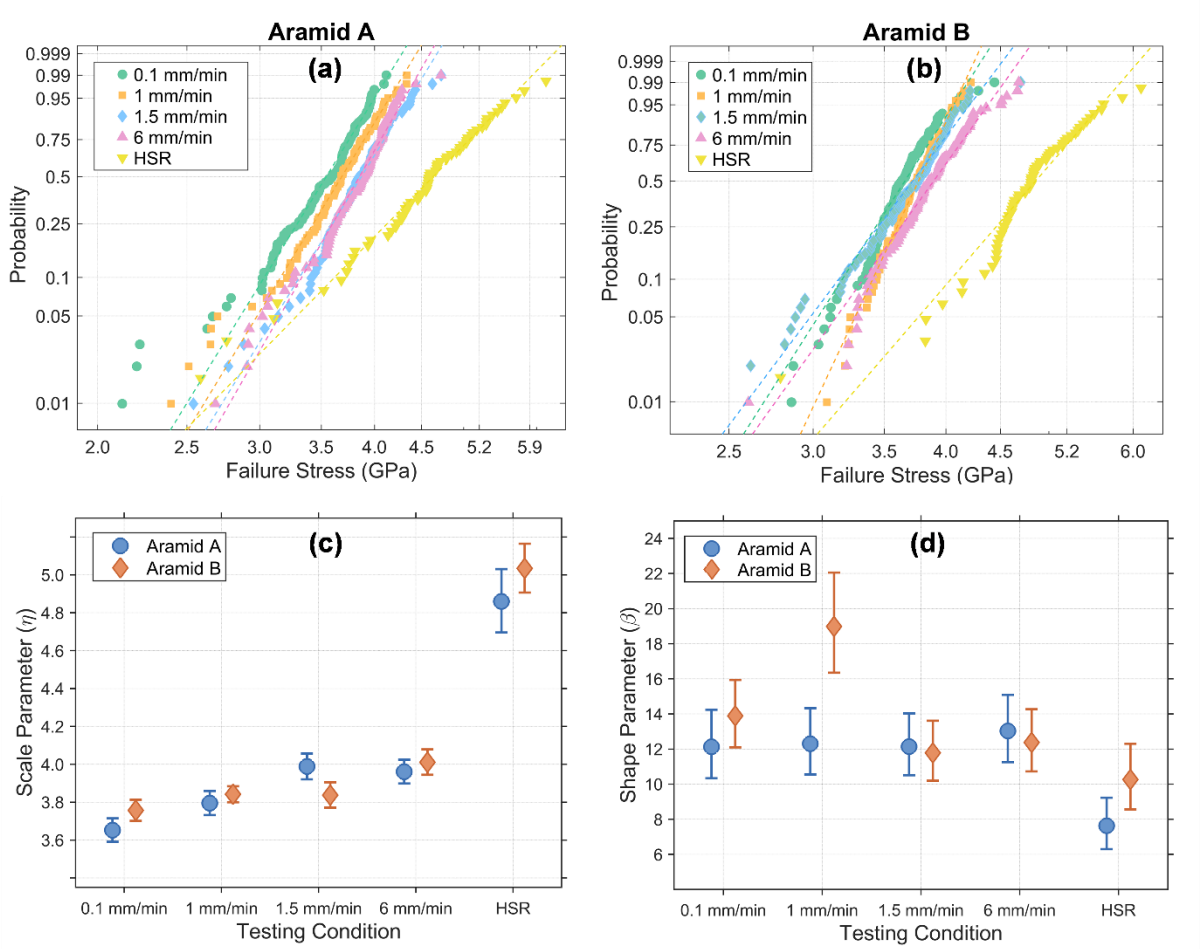

Figure 9: (a-b) Two-parameter Weibull probability plots of failure stress for Aramid A and Aramid B fibers tested under five different testing conditions (0.1, 1, 1.5, 6 mm/min, and HSR), corresponding to nominal strain rates of [1.1×10^{-4}, 1.1×10^{-3}, 1.7×10^{-3}, 6.7×10^{-3}] s^{-1}, respectively) and the HSR condition (370 s^{-1}). Dashed lines represent Weibull fits to the data. (c-d) Weibull scale (η) and shape (β) parameters with 95 % CI for both fibers as a function of testing condition.

Results obtained at all QS testing conditions for both fiber types demonstrate a good fit to the two-parameter Weibull model. For Aramid B at a rate of 1 mm/min, β is comparatively higher, which corresponds to the strong fit and shorter lower-tail behavior. The same elevation appears in the failure strain distribution, which is expected since both properties were measured on the same specimens. As discussed in Section 3.2.1, it is attributed to sampling variability rather than a rate-dependent effect. Under HSR loading, Aramid A continues to show an approximately linear fit to the model. In contrast, at HSR loading, Aramid B shows a slight deviation from the fitted line in the lower-tail region, meaning a few low-stress points deviate from the ideal two-parameter linear trend. Additionally, the HSR results for Aramid A exhibit a more gradual slope compared to the steeper slopes seen in the QS curves, indicating a greater spread in failure stress at HSR loading (i.e., lower β and higher dispersion). This may be partially attributable to the increased scatter in strain rates for the Kolsky bar compared to the FAVIMAT+. Additionally, because failure stress is a derived quantity calculated from both the measured force and the estimated cross-sectional area, variability from both sources adds to the stress calculation, which may further broaden the failure stress distribution relative to directly measured properties.

Table 5 includes the distributional trends and the strain-rate effect reflected by the scale parameter η in Figure 9(c). The mean failure stress under HSR loading increases relative to QS testing conditions, and the scatter increases at HSR. For example, the SD for Aramid A increases from approximately 0.36 GPa to 0.39 GPa in the QS groups to 0.71 GPa under HSR (CV rising from 9 % to 11 % to 16 %). For Aramid B, SD ranges from approximately 0.23 GPa to 0.39 GPa across the QS groups, increasing to 0.52 GPa under HSR. Overall, these results indicate that failure stress increases with strain rates, confirming the strain rate effect similarly to failure strain, while the distribution of failure stress becomes moderately broader at the HSR testing condition, especially for Aramid A.

3.3.2 Statistical Analysis

Figure 10 displays failure stress as a function of testing conditions for Aramid A and B fibers across QS and HSR testing conditions. Similar to failure strain, the results obtained under HSR loading in both fibers show higher medians and wider IQRs, indicating higher average failure stress and greater variability at HSR. The spread is more pronounced for Aramid A as seen from the whiskers and IQR, which are consistent with the broader Weibull slope and lower shape parameter (β) under HSR loading seen in Figure 9(c-d). In contrast, the Aramid B HSR distribution is tighter than Aramid A, indicating a more uniform stress response across strain rates. This behavior is consistent with the lower baseline variability observed in Aramid B linear density and suggests fewer variations in filament-level geometry or defect population.

Within the QS testing conditions, a slight upward shift in the median failure stress relative to the 0.1 mm/min condition is observed. However, the box plots for the closely spaced QS testing conditions largely overlap. Therefore, the strain rate effect within the QS range is visually subtle. The post hoc analysis in Table 6 highlights a key distinction from failure strain. Failure stress shows additional statistically significant differences within the QS regime, even within relatively close rates. The relatively large sample size provides statistical power to observe such differences. For example, significant differences were identified between 0.1 vs. 1.5 mm/min, 0.1 vs. 6 mm/min and 1 vs. 1.5 mm/min for Aramid A. For Aramid B, significant differences were observed between 0.1 vs. 6 mm/min only. Failure stress appears to be more sensitive to subtle QS testing conditions differences than failure strain.

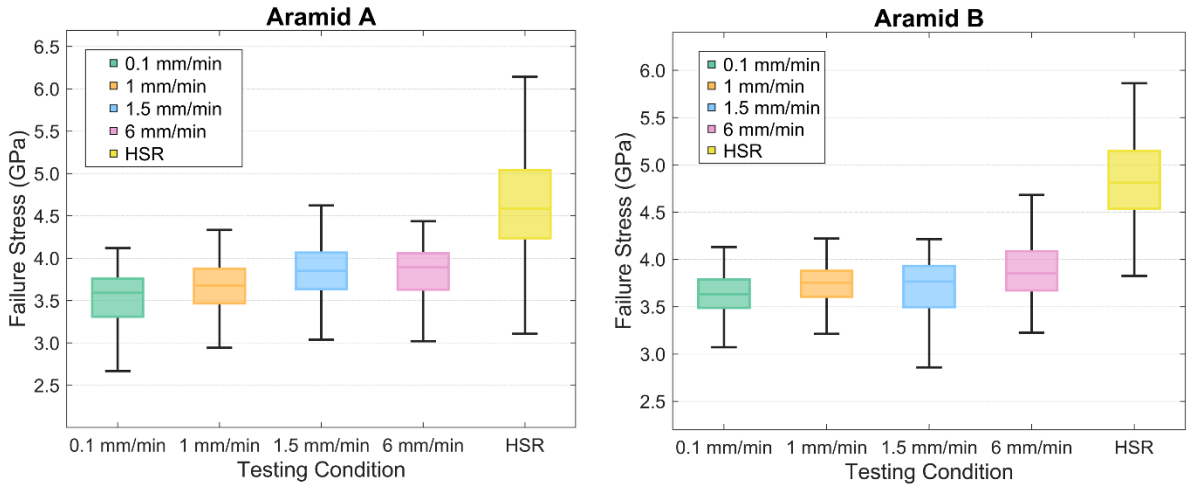

Figure 10: Box plots of failure stress for Aramid A and Aramid B across five different testing conditions ([0.1, 1, 1.5, 6] mm/min, and HSR), corresponding to nominal strain rates of [1.1 × 10^{-4}, 1.1 × 10^{-3}, 1.7 × 10^{-3}, 6.7 × 10^{-3}] s^{-1}, respectively) and the HSR condition (370 s^{-1}). The central line represents the median, the lower and upper box edges represent the 25th and 75th percentiles (IQR). The whiskers extend to the most extreme data points within 1.5 × IQR from the box edges. Outliers beyond the whiskers are not displayed.

The FAVIMAT+ system provides highly precise measurements of force and precisely controls the gauge length and gripping. In addition, results from Figure 6 show that linear density was consistent across all testing condition groups. Therefore, it is unlikely that the additional differences observed between some QS groups arise from instrumental error or sample selection bias. Instead, the differences may reflect the intrinsic material variability and inherent sensitivity of failure stress as a derived metric. Because failure stress is calculated by normalizing force with linear density, the computation can amplify the effects of small fiber-level variations, such as defects, fibril misalignment, or local stress concentrations. The influences may not be as visible when looking only at failure strain. However, under the more conservative significance threshold (p = 0.01), these within-QS differences are limited to only a few pairwise comparisons, indicating that any rate-dependent effect within the QS regime is subtle rather than systematic across all testing conditions. Thus, the results suggest some sensitivity of failure stress to QS testing conditions, but the effect appears modest.

The 31 % to 32 % increase in failure stress at HSR observed in the present study is notably larger than most previously reported values for single aramid fibers tested using Kolsky-type setups. For example,

Cheng et al. [19] reported only an approximately 4 % increase for Kevlar KM2 fiber. Kim et al. [18] observed approximately 14 % for Kevlar 29, and Lim et al. [16] found between 6 % to 12 % across three aramid fiber types. Sanborn and Weerasooriya [20] reported an 18.6 % increase for unwoven Kevlar KM2 fibers. Several methodological factors may contribute to the larger effect observed in this study. The present study used substantially larger sample sizes (n = 62 per fiber under HSR, n = 100 per QS condition), PMMA mechanical clamp grips that reduce grip-induced compliance [31] compared to adhesive glue-tab methods used in prior studies, and a paper frame templating technique to minimize slack and gauge-length artifacts. Additionally, failure strain was measured directly via DIC rather than estimated from bar signals, and failure stress was derived using a paired-sampling approach with propagated uncertainty. Direct comparisons across studies are limited by differences in exact fiber type, gauge length, strain rate, and instrument configurations. Nevertheless, the consistency of the rate-dependent response across all three measured properties supports that the observed strain rate effects reflect intrinsic material behavior.

Beyond the failure stress and failure strain that are the focus of this study, the initial modulus was also calculated for the QS conditions from the linear region of the stress-strain response. For both fibers, the modulus ranged from approximately 104 GPa to 111 GPa (Table S7), with low scatter (CV ≈ 4 % to 7 %) and only slightly increased with strain rate. The initial modulus could not be reliably determined under HSR conditions, as discussed in Supplementary Section S2.4.

4. Conclusion

The study presents a comprehensive investigation into the strain-rate-dependent mechanical behavior of two aramid fibers, Aramid A (Kevlar) and Aramid B (Twaron), under both QS and HSR loading. Using a modified Mini-Kolsky tension bar with rigid-body DIC grip tracking, relative grip displacement was directly tracked to calculate strain at failure. Across both fiber types, significant strain rate effects were observed. Specifically, 28.5 % to 35.6 % increases in maximum force, failure strain, and failure stress at HSR were observed in comparison to the results obtained at the slowest QS testing condition (0.1 mm/min). Even within the nominally QS range (0.1 mm/min to 6 mm/min), modest increases of 6 % to 10 % in failure stress were observed between the lowest and highest rates, while failure strain showed no systematic trend within the QS regime. The observed increases in both failure stress and failure strain at HSR are consistent with the rigid-rod microstructure of PPTA, where the dominant failure mechanism transitions from inter-chain slippage at low rates to primary covalent bond scission at high rates. This transition requires greater strain energy before failure, resulting in higher failure strains and stresses under HSR loading. The findings are larger in magnitude than the 4 % to 19 % increases reported in prior single-fiber aramid studies, which may be attributed in part to the larger sample sizes, direct strain measurement, and improved gripping methodology employed in the present work. Since ballistic impacts on body armor can impose strain rates comparable to, or higher than, those achieved here, HSR characterization at this range and above is essential for accurately predicting ballistic performance of aramid fibers. Relying solely on QS single-fiber properties may not adequately capture the rate-dependent response that governs fiber behavior during ballistic events. Future work should focus on refining single-fiber HSR testing capabilities, including improvements to the striker mechanism and pulse-shaping strategies for more uniform strain-rate control, and increasing strain rates toward the higher rates encountered in ballistic events. Another avenue is to explore direct strain measurement on the fiber itself to complement the rigid-body grip tracking approach used here.

5. CRediT Author Statement

Atik Faisal: Writing - Original Draft, Writing - Review & Editing, Formal Analysis, Investigation, Conceptualization. **Alexander K Landauer:** Methodology, Supervision, Writing - Review & Editing. **Wally Adamy**: Writing - Review & Editing, Investigation. **Dumbari David Kabari**: Writing - Review & Editing. **Amanda L. Forster:** Writing - Review & Editing, Supervision. **Amy Engelbrecht-Wiggans:** Supervision, Project administration, Methodology, Funding acquisition, Conceptualization. **Kathleen Lamkin-Kennard:** Writing - Review & Editing, Supervision, Formal analysis.

6. Funding

Kathleen Lamkin-Kennard reports financial support, administrative support, article publishing charges, travel, and writing assistance were provided by National Institute of Standards and Technology through award number 70NANB23H035. Atik Faisal reports a relationship with Rochester Institute of Technology that includes: employment and funding grants. Other authors declare that they have no known competing financial interests or personal relationships that could have appeared to influence the work reported in this paper.

7. Acknowledgments

The authors would like to acknowledge Nicolas Paulter and John Jendzurski, for their assistance in setting up the Kolsky bar, and Michael A. Riley for his help in setting up the high-speed camera system with the Kolsky bar.

8. Conflict of Interest

The authors declare that they have no conflicts of interest.

9. Disclaimers

The opinions, recommendations, findings, and conclusions in the manuscript do not necessarily reflect the views or policies of NIST or the United States Government.

Certain commercial equipment, instruments, or materials are identified in this paper in order to specify the experimental procedure adequately. Such identification is not intended to imply recommendation or endorsement by NIST, nor is it intended to imply that the materials or equipment identified are necessarily the best available for the purpose.

10.Data availability

All data supporting this work are published and available from the NIST Public Data Repository [37] at the following link https://doi.org/10.18434/mds2-4163.

11. References

[1] "Body Armor: Protecting Our Nation's Officers From Ballistic Threats | National Institute of Justice." Accessed: Mar. 19, 2026. [Online]. Available: https://nij.ojp.gov/topics/articles/body-armor-protecting-our-nations-officers-ballistic-threats

[2] "Standard Test Method for Collection of Ballistic Limit Data for Ballistic-resistant Torso Body Armor and Shoot Packs," Mar. 2018, doi: 10.1520/E3110-18.

[3] D. Ahmed, Z. Hongpeng, K. Haijuan, L. Jing, M. Yu, and Y. Muhuo, "Microstructural developments of poly (p-phenylene terephthalamide) fibers during heat treatment process: a review," *Materials Research*, vol. 17, no. 5, pp. 1180–1200, Sep. 2014, doi: 10.1590/1516-1439.250313.

[4] M. Akbarian, S. Hassanzadeh, and M. Moghri, "Short Twaron aramid fiber reinforced thermoplastic polyurethane," *Polym. Adv. Technol.*, vol. 19, no. 12, pp. 1894–1900, Dec. 2008, doi: 10.1002/pat.1225.

[5] S. Chowdhury, R. B. Austin, and M. A. Ford, "Limiting role of crystalline domain orientation on the modulus and strength of aramid fibers," *Polymer (Guildf).*, vol. 140, no. 2, pp. 96–106, Mar. 2018, doi: 10.1017/S0021859600085038.

[6] Y. Rao, A. J. Waddon, and R. J. Farris, "Structure–property relation in poly(p-phenylene terephthalamide) (PPTA) fibers," *Polymer (Guildf).*, vol. 42, no. 13, pp. 5937–5946, Jun. 2001, doi: 10.1016/S0032-3861(00)00905-8.

[7] S. Bourbigot, X. Flambard, and F. Poutch, "Study of the thermal degradation of high performance fibres—application to polybenzazole and p-aramid fibres," *Polym. Degrad. Stab.*, vol. 74, no. 2, pp. 283–290, Jan. 2001, doi: 10.1016/S0141-3910(01)00159-8.

[8] S. Sockalingam, S. C. Chowdhury, J. W. Gillespie, and M. Keefe, "Recent advances in modeling and experiments of Kevlar ballistic fibrils, fibers, yarns and flexible woven textile fabrics – a review," *Textile Research Journal*, vol. 87, no. 8, pp. 984–1010, May 2017, doi: 10.1177/0040517516646039.

[9] S. Leigh Phoenix and P. K. Porwal, "A new membrane model for the ballistic impact response and V50 performance of multi-ply fibrous systems," *Int. J. Solids Struct.*, vol. 40, no. 24, pp. 6723–6765, Dec. 2003, doi: 10.1016/S0020-7683(03)00329-9.

[10] M. Hudspeth, D. Li, J. Spatola, W. Chen, and J. Zheng, "The effects of off-axis transverse deflection loading on the failure strain of various high-performance fibers," *Textile Research Journal*, vol. 86, no. 9, pp. 897–910, Jun. 2016, doi: 10.1177/0040517515588262

[11] S. Sockalingam, J. W. Gillespie, and M. Keefe, "Role of Inelastic Transverse Compressive Behavior and Multiaxial Loading on the Transverse Impact of Kevlar KM2 Single Fiber," *Fibers 2017, Vol. 5, Page 9*, vol. 5, no. 1, p. 9, Feb. 2017, doi: 10.3390/FIB5010009.

[12] S. J. Deteresa, S. R. Allen, R. J. Farris, and R. S. Porter, "Compressive and torsional behaviour of Kevlar 49 fibre," *Journal of Materials Science 1984 19:1*, vol. 19, no. 1, pp. 57–72, 1984, doi: 10.1007/BF02403111.

[13] M. G. Dobb, D. J. Johnson, and B. P. Saville, "Compressional behaviour of Kevlar fibres," *Polymer (Guildf).*, vol. 22, no. 7, pp. 960–965, Jul. 1981, doi: 10.1016/0032-3861(81)90276-7.

[14] W. Chen and B. Song, "Split Hopkinson (Kolsky) Bar," 2011, doi: 10.1007/978-1-4419-7982-7.

[15] H. Wang *et al.*, “Tensile properties of ultra-high-molecular-weight polyethylene single yarns at different strain rates,” *J. Compos. Mater.*, vol. 54, no. 11, pp. 1453–1466, May 2020, doi: 10.1177/0021998319883416.

[16] J. Lim, J. Q. Zheng, K. Masters, and W. W. Chen, “Effects of gage length, loading rates, and damage on the strength of PPTA fibers,” *Int. J. Impact Eng.*, vol. 38, no. 4, pp. 219–227, Apr. 2011, doi: 10.1016/j.ijimpeng.2010.11.009.

[17] D. Zhu, B. Mobasher, J. Erni, S. Bansal, and S. D. Rajan, “Strain rate and gage length effects on tensile behavior of Kevlar 49 single yarn,” *Compos. Part A Appl. Sci. Manuf.*, vol. 43, no. 11, pp. 2021–2029, Nov. 2012, doi: 10.1016/j.compositesa.2012.06.007.

[18] J. H. Kim *et al.*, “Statistical analysis of PPTA fiber strengths measured under high strain rate condition,” *Compos. Sci. Technol.*, vol. 98, pp. 93–99, Jun. 2014, doi: 10.1016/j.compscitech.2012.03.021.

[19] M. Cheng, W. Chen, and T. Weerasooriya, “Mechanical Properties of Kevlar® KM2 Single Fiber,” *J. Eng. Mater. Technol.*, vol. 127, no. 2, pp. 197–203, Apr. 2005, doi: 10.1115/1.1857937.

[20] B. Sanborn and T. Weerasooriya, “Quantifying damage at multiple loading rates to Kevlar KM2 fibers due to weaving, finishing, and pre-twist,” *Int. J. Impact Eng.*, vol. 71, no. 17, pp. 50–59, Sep. 2014, doi: 10.1016/j.ijimpeng.2014.04.005.

[21] H. H. . Yang, *Kevlar Aramid Fiber*, 1st ed. J. Wiley, 1993.

[22] J. H. Kim *et al.*, “Effect of fiber gripping method on the single fiber tensile test: II. Comparison of fiber gripping materials and loading rates,” *Journal of Materials Science 2014 50:5*, vol. 50, no. 5, pp. 2049–2060, Dec. 2014, doi: 10.1007/s10853-014-8736-8.

[23] B. Mercer, E. Zywicz, and P. Papadopoulos, “Molecular dynamics modeling of PPTA crystallite mechanical properties in the presence of defects,” *Polymer (Guildf).*, vol. 114, no. 58, pp. 329–347, Apr. 2017, doi: 10.1016/j.polymer.2017.03.012.

[24] V. B. C. Tan, X. S. Zeng, and V. P. W. Shim, “Characterization and constitutive modeling of aramid fibers at high strain rates,” *Int. J. Impact Eng.*, vol. 35, no. 11, pp. 1303–1313, Nov. 2008, doi: 10.1016/j.ijimpeng.2007.07.010.

[25] R. L. Rhorer, J. H. Kim, and S. P. Mates, “NIST Mini-Kolsky Bar: Historical review,” *Conference Proceedings of the Society for Experimental Mechanics Series*, vol. 1B, pp. 177–183, Aug. 2017, doi: 10.1007/978-3-319-41132-3_25.

[26] D. Olteanu and L. Freeman, “The evaluation of median-rank regression and maximum likelihood estimation techniques for a two-parameter Weibull distribution,” *Qual. Eng.*, vol. 22, no. 4, pp. 256–272, Oct. 2010, doi: 10.1080/08982112.2010.505219.

[27] A. Faisal, D. D. Kabari, B. Doolin, A. L. Forster, and A. Engelbrecht-Wiggans, “Intra versus inter fiber variability in mechanical properties of high-performance fibers,” *Composites Part C: Open Access*, p. 100742, May 2026, doi: 10.1016/J.JCOMC.2026.100742.

[28] A. Engelbrecht-Wiggans *et al.*, “Effects of temperature and humidity on high-strength p-aramid fibers used in body armor,” *Textile Research Journal*, vol. 90, no. 21–22, pp. 2428–2440, Nov. 2020, doi: 10.1177/0040517520918232.

[29] A. K. Landauer, M. Patel, D. L. Henann, and C. Franck, “A q-Factor-Based Digital Image Correlation Algorithm (qDIC) for Resolving Finite Deformations with Degenerate Speckle Patterns,” *Experimental Mechanics 2018 58:5*, vol. 58, no. 5, pp. 815–830, Mar. 2018, doi: 10.1007/s11340-018-0377-4.

[30] A. E. Engelbrecht-Wiggans and A. L. Forster, “Analysis of strain correction procedures for single fiber tensile testing,” *Compos. Part A Appl. Sci. Manuf.*, vol. 167, p. 107411, Apr. 2023, doi: 10.1016/j.compositesa.2022.107411.

[31] D. R. Jenket, A. E. Engelbrecht-Wiggans, A. L. Forster, and M. Al-Sheikhly, “A new method for tensile testing UHMMPE single fibers at high temperatures and strain-rates,” *NISTIR 8265*, 2019, doi: 10.6028/NIST.IR.8265.

[32] S. Koumlis and L. Lamberson, “Strain Rate Dependent Compressive Response of Open Cell Polyurethane Foam,” *Exp. Mech.*, vol. 59, no. 7, pp. 1087–1103, Sep. 2019, doi: 10.1007/s11340-019-00521-3.

[33] J. I. Perry and · S M Walley, “Measuring the Effect of Strain Rate on Deformation and Damage in Fibre-Reinforced Composites: A Review,” *Journal of Dynamic Behavior of Materials*, vol. 8, pp. 178–213, 2022, doi: 10.1007/s40870-022-00331-0.

[34] S. L. PHOENIX and I. J. BEYERLEIN, “Statistical Strength Theory for Fibrous Composite Materials,” *Comprehensive Composite Materials*, pp. 559–639, Jan. 2000, doi: 10.1016/b0-08-042993-9/00056-5.

[35] R. Jiang and D. N. P. Murthy, “A study of Weibull shape parameter: Properties and significance,” *Reliab. Eng. Syst. Saf.*, vol. 96, no. 12, pp. 1619–1626, Dec. 2011, doi: 10.1016/j.ress.2011.09.003.

[36] T. Rahmani, B. Kiani, M. Shekarchi, and A. Safari, “Statistical and experimental analysis on the behavior of fiber reinforced concretes subjected to drop weight test,” *Constr. Build. Mater.*, vol. 37, pp. 360–369, Dec. 2012, doi: 10.1016/j.conbuildmat.2012.07.068.

[37] A. Faisal, W. J. Adamy, A. L. Forster, A. Engelbrecht-Wiggans, and Alexander K, “Data for Revealing Statistically Robust Strain Rate Effects on the Mechanical Performance of Pristine Single Fiber Aramids,” 2026. doi: 10.18434/mds2-4163.